Use of ZDR columns for early detection of severe convection within the operational radar network of the United Kingdom

Received: 10 February 2023 | Revised: 26 September 2023 | Accepted: 14 October 2023

DOI: 10.1002/met.2159

Meteorological Applications
Science and Technology for Weather and Climate
Open Access
RMetS

RESEARCH ARTICLE

Use of Z_{DR} columns for early detection of severe convection within the operational radar network of the United Kingdom

Chun Hay Brian Lo[1] | **Thorwald H. M. Stein**[1] | **Robert W. Scovell**[2] | **Chris D. Westbrook**[1] | **Timothy Darlington**[2] | **Humphrey W. Lean**[3]

[1]Department of Meteorology, University of Reading, Reading, UK

[2]Met Office, Exeter, UK

[3]MetOffice@Reading, Reading, UK

Correspondence
Thorwald H. M. Stein, Department of Meteorology, University of Reading, Reading, UK.
Email: t.h.m.stein@reading.ac.uk

Funding information
University of Reading Department of Meteorology PhD Scholarship

Abstract

Differential reflectivity (Z_{DR}) columns were observed using a Met Office three-dimensional radar composite. An algorithm for automatic detection of Z_{DR} columns was developed, based on $Z_{DR} \geq 1.0$ dB and $Z_H \geq 10$ dBZ. Across three case days, detected Z_{DR} columns were found to precede severe convection in tracked convective cells with a range of lead times from 0 to 20 min depending on the case day. Requiring maxima above 1.4 dB and 30 dBZ of Z_{DR} and Z_H respectively was an appropriate second condition for all three cases although the skill in the early detection of severe convection varied across case days. Despite the high probability of detections, the high false alarm rate accompanied by low critical success index and data latency limit performance based on the three cases considered in this study. Nevertheless, the ability to detect Z_{DR} columns in operational radar data with a useful lead time prior to severe convection in certain conditions is a promising development towards advancing nowcasting of severe convection in the United Kingdom.

KEYWORDS

nowcasting, polarimetric radar

1 | INTRODUCTION

A differential reflectivity (Z_{DR}) column is defined as "a region of enhanced Z_{DR} as situated above the 0°C level" (Kumjian, 2013) that can be identified from weather radar measurements. Z_{DR}, which is defined as the difference in dB between the horizontally and vertically polarized radar reflectivity, Z_H and Z_V, is generally a measure of the sphericity of radar targets for which the Rayleigh approximation is valid. More positive values indicate more oblate shapes, although for large hydrometeors, Mie resonance scattering effects could disrupt the relationship between aspect ratio and Z_{DR}. The majority makeup of a Z_{DR} column is raindrops at its base and wet hail with supercooled raindrops or those in the process of freezing near the middle and upper sections of the column (Kumjian et al., 2014; Snyder et al., 2015). As such, a Z_{DR} column is indicative of a strong updraft that would support the lofting of these large oblate drops. Although ice crystals such as dendrites and plates can also enhance Z_{DR}, these tend to have small Z_H values and can thus be discriminated from large raindrops (e.g. Hogan et al., 2002,

2003; Westbrook et al., 2010). When the concentration of large raindrops is low, a Z_{DR} column may have small Z_H value too, in which case further context such as temperature, storm evolution and vertical extent of the column will help distinguish the signature from ice crystals.

Z_{DR} columns have been widely documented in the literature, starting from early polarimetric radar observations (e.g. Illingworth et al., 1987). They have been related to areas near or at updraft maxima (e.g. Kumjian et al., 2014; Kumjian & Ryzhkov, 2008; Snyder et al., 2015, 2017) as shown conceptually in Figure 1a. Brandes et al. (1995) showed using in situ aircraft measurements through a limited number of convective cells that the observed Z_{DR} columns were dominated by large liquid drops and mixed-phased precipitation near the top of Z_{DR} columns as labelled in Figure 1b. As illustrated in Figure 1c, Herzegh and Jameson (1992) have found both heavy rain and hail polarimetric signatures in a mature convective cell following the manifestation of a Z_{DR} column. More recently, studies have highlighted the importance and usefulness of Z_{DR} columns in informing forecast warning decisions, compared with only utilizing reflectivity signatures (e.g. Kuster et al., 2019, 2020).

The UK Met Office has fully upgraded all 15 C-band radars as of January 2018 to have polarimetric capabilities. Three-dimensional radar composite products that incorporate the whole UK radar network, originally developed for the European SESAR Aviation programme, provide large horizontal spatial coverage on the order of 1000 km (Scovell & Al-Sakka, 2016). Whereas a single radar would only be able to detect hydrometeors as high as its highest elevation, thus leaving the so-called "cone of silence" aloft closest to the radar, the dense UK network permits nearby radars to fill in these regions of missing observations. The 3D vertical structure provides important information for aviation meteorology where pilots navigate to avoid areas of severe convective development (Scovell & Al-Sakka, 2016). It also complements existing surface rainfall rate products (Harrison et al., 2009) for nowcasting severe convection over the entirety of the United Kingdom that could cause flooding, which could be used as a central component of a national severe convection nowcasting system. Stein et al. (2020) verified the reliability of the 3D composite by comparison with data from the Chilbolton Advanced Meteorological Radar (CAMRa) using cloud-top height, fractional coverage and storm morphology, all with reflectivity thresholds for studying convective storm characteristics.

The use of Z_{DR} for nowcasting is currently only explored in a few countries. The effectiveness of Z_{DR} columns detection for the United Kingdom is yet to be explored. Plummer et al. (2018) studied Z_{DR} signatures in warm-based convective cases (i.e., convective events for which the inflow source originates from levels warmer than freezing point) from the summer of 2013 Convective Precipitation Experiment (COPE) field campaign. Using data from a mobile X-band radar, they showed that larger derived precipitation rates were associated with convective systems containing Z_{DR} columns. However, cases studied in Plummer et al. (2018) had access to a research radar that scanned at 10 elevation angles, as opposed to the 5 angles used operationally. It is not self-evident that Z_{DR} columns can be used for nowcasting based on these findings alone. Furthermore, their results may partly be influenced by the unique topography of the south-west peninsula that inspired the COPE campaign.

To harness the greater spatial domain of the 3D radar composite constituting data from multiple overlapping radars, for this study, it was upgraded to include Z_{DR} to

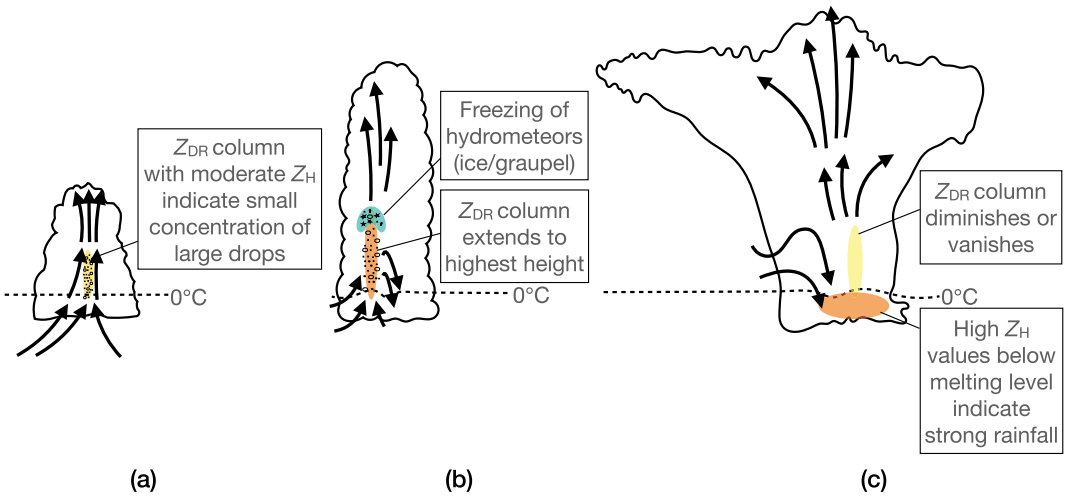

FIGURE 1 Conceptual diagrams showing the (a) developing (b) vigorous growth and (c) mature stages of a convective cell focusing on Z_{DR} column evolution.

investigate the operational potential of using Z_{DR} columns for nowcasting severe convection. This study assesses the effectiveness of an implemented threshold-based Z_{DR} column detection algorithm for diagnosing severe convective development across three different case days within the United Kingdom.

Cases studied are introduced in the next section (Section 2), followed by a description of the data used and a description of the Z_{DR} column detection algorithm in Section 3 including an analysis of sensitivity to threshold values. Results pertaining to specific convective cells, lead time and verification of the algorithm's accuracy in nowcasting severe storms are detailed in Section 4. A discussion and conclusion are presented in the final section (Section 5).

2 | CASES OF SEVERE CONVECTION

2.1 | Radar-based definition of severe convection in the United Kingdom

In order to diagnose whether a tracked storm cell eventually develops into a "severe" storm, we need a quantitative definition of what constitutes a severe storm. In this study, we have chosen to define this based upon counting the accumulated number of high-reflectivity MAXDBZ pixels within each tracked cell. The quantity MAXDBZ is the vertical maximum of radar reflectivity Z_H. In the radar composite, a single pixel covers an area of 1×1 km, and a time frame of 5 min. An accumulated number of 12 pixels could thus be a storm with a single pixel above the threshold persisting for 1 h, or a storm with 12 pixels above the threshold lasting only 5 min (and any scenario between these extremes). Having analysed all tracked storms across our three case studies, we find that 50 accumulated pixels of MAXDBZ values that are greater than or equal to 50 dBZ correspond well to the 99th percentile of accumulated MAXDBZ pixels across tracked cells. Thus, 50 accumulated 50 dBZ pixels in the MAXDBZ field are selected as a criterion for labelling a tracked storm as severe in this study. A physical interpretation of 50 accumulated pixels of 50 dBZ is 2.0×10^8 kg of rain or having a depth of 204 mm if it were concentrated in a 1 km^2 surface, assuming the Marshall–Palmer relationship (Marshall et al., 1947) for converting reflectivity to rainfall.

In contrast to the United States, where the definition of a severe thunderstorm is one that produces hail with diameters equal to or larger than an inch, wind gusts that exceed 58 mph and/or produce a tornado (National Weather Service, 2017), the United Kingdom does not have such a definition and hardly experiences inch-sized hail. In the United Kingdom, severe thunderstorms are marked by heavy precipitation, which are associated with sustained high-reflectivity pixels within an evolving convective cell. This justifies the choice of using accumulated MAXDBZ as a metric as opposed to very high reflectivity cores for large hail diagnosis or Doppler signals that would indicate strong gusts.

2.2 | Cases

To develop and test the Z_{DR} column detection algorithm, three cases were selected from the European Severe Weather Database (Dotzek et al., 2009) with news reports of heavy rain or hail associated with severe convective events in the United Kingdom.

On 16 June 2020, multiple intense isolated cells resulted in cases of damaging lightning and heavy rain over the West Midlands. The sounding on that day is shown in Figure 2a and is characterized by moderate instability with convective available potential energy (CAPE) of around 1300 Jkg^{-1}. The sounding profile presents an unstable surface layer and a moist surface to mid-level, up to 600 hPa. A moderate bulk wind shear of 11 ms^{-1} from surface to 6 km accompanied with a positive vorticity filament aloft that would have promoted dynamical ascent via differential positive vorticity advection likely supported convective development (not shown). The bulk Richardson number was approximately 100, placing the storm environment within the single or multi-cell storms regime (Weisman & Klemp, 1982).

On 10 August 2020, multiple cells formed in south-western England, which developed into a mesoscale convective system and advected northwards to parts of Wales. Cases of damaging lightning and heavy rain were recorded in parts of Wales including Swansea. The sounding shown in Figure 2c has CAPE reaching 850 J kg^{-1} when considering ascent of the most unstable parcel. Surface heating later during the day (not shown) would have contributed to more instability. Similar to 16 June 2020, a positive vorticity filament aloft in the afternoon hours would have supported convective development. The bulk wind shear of 4 ms^{-1} gives a bulk Richardson number of around 100, similar to that of the June case.

On the afternoon of 20 July 2021, isolated cells formed over East England and East Midlands, evolving into a multi-cell system towards the evening and finally dissipating before midnight. Multiple cases of flooding and hail were recorded for different locations in England between 14 and 17Z. The sounding for this case is presented in Figure 6 with CAPE exceeding 1600 Jkg^{-1}. There was also a highly positive area of vorticity aloft during the afternoon hours of this case. The bulk wind shear of 4 ms^{-1} gives a bulk Richardson number of around 200.

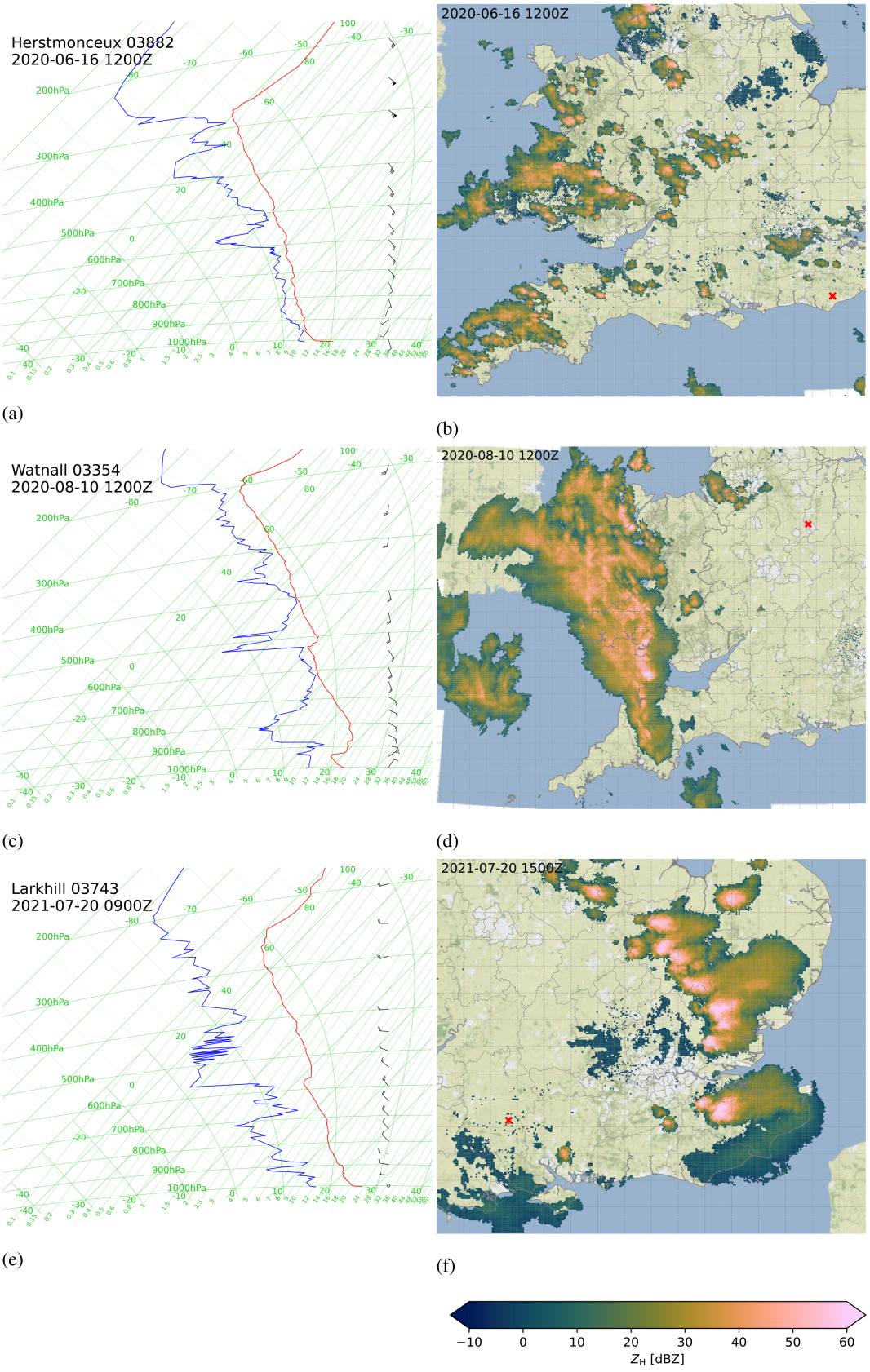

FIGURE 2 Tephigrams showing reported sounding data from (a) Herstmonceux on 16 June 2020 at 1200Z, (c) Watnall on 10 August 2020 at 1200Z and (e) Larkhill on 20 July 2021 at 0900Z. Blue and red lines correspond to dewpoint and dry bulb temperature. Wind barbs are plotted on the right side at selected pressure levels. Maximum reflectivity plots (b), (d) and (f) show a snapshot of radar echoes present on the same case days as the tephigrams in (a), (c) and (e), respectively. The red cross on each plot shows the location of the radiosonde launch. Map tiles by Stamen Design, under CC BY 4.0. Data by OpenStreetMap, under ODbL.

The three chosen case days present a variety of radar echo sizes and organisations as seen in Figure 2b,d,f. Locations of the described radiosonde launches are marked as red crosses in the same figures. Convective cells within these three case days introduced are tracked and investigated in this study.

3 | DATA AND METHODOLOGY

3.1 | UK 3D radar composite

The UK Met Office operational radar network is comprised of 16 C-band radars. Fifteen of these radars are located within the United Kingdom and one is on the Channel Islands. All C-band radars have been fully upgraded as of January 2018 to have dual-polarization capabilities. Each radar completes a set of plan-position indicator (PPI) scans at elevations 0.5, 1.0, 2.0, 3.0 and 4.0 degrees approximately every 5 min. The radars have a pulse repetition frequency of 300 Hz and a scan velocity of 8.4 degrees per second for the lowest two elevations and 15 degrees per second for the higher elevations. Depending on the rotation rate, a variable number of pulses are integrated and averaged once an integer degree boundary is crossed. Each PPI scan covers a range of 255 km, has range gates of 600 m and a radar beamwidth of 1.0°.

In this study, multi-radar composites were generated using various configurations of the Hameldon Hill, Ingham, Clee Hill, Crug-y-Gorllwyn, Chenies, Thurnham, Cobbacombe Cross, Dean Hill and Predannack Met Office radars. The locations of these radars and others in the network are shown in Figure 3. These nine radars provide coverage of convective storms over southern England and Wales, coincident with the severe weather observations described in Section 2. The use of data from multiple radars helps to cover the "cone of silence" that is not sampled by the highest and lowest elevation scans from a single radar. Scovell and Al-Sakka (2016) show that a 1 km^3 volume intersected by different 3 dB radar beams results in up to 17 available observations from multiple UK radar volumes.

Following Scovell and Al-Sakka (2016), the radar data are interpolated onto a three-dimensional Cartesian grid, with 1 km horizontal and 500 m vertical spacing. Advection corrections are applied before compositing, using motion vectors derived from the previous two radar composites. In places where the radars overlap, a range-dependent weighting scheme of Zhang et al. (2005) is used. Finally, vertical linear interpolation is carried out at the request point. This study extends the described compositing process to the Z_{DR} field, by employing a similar method of interpolating Z_{DR} in dB units.

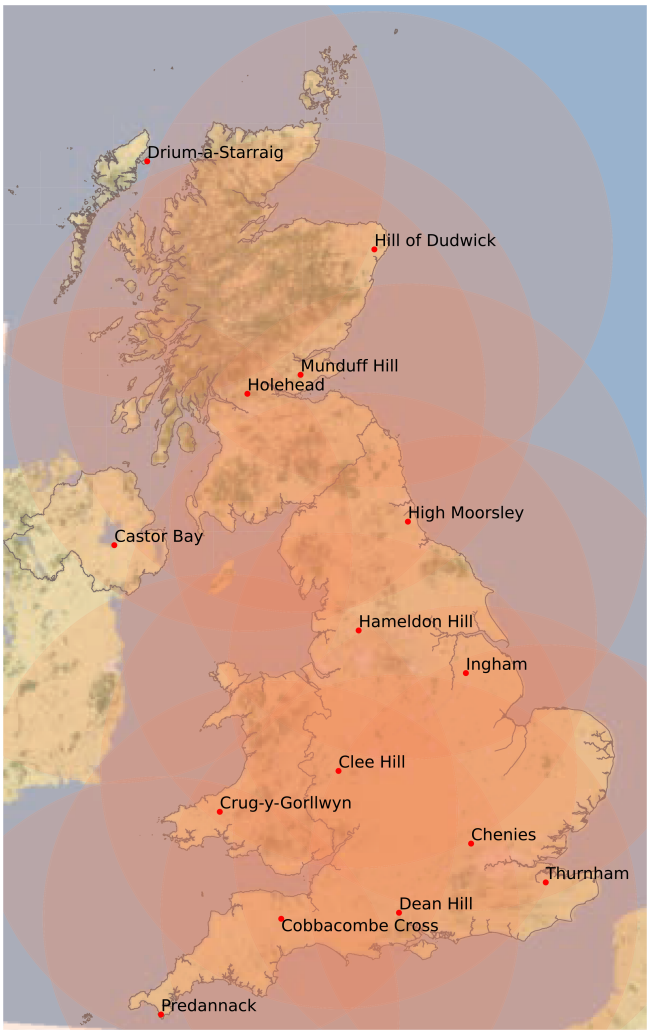

FIGURE 3 An overview of UK Met Office C-band radar locations and names. Range rings of 255 km are included around each radar site. Map tiles by Stamen Design, under CC BY 4.0. Data by OpenStreetMap, under ODbL.

3.2 | Cell identification

Individual convective cells are identified from the MAXDBZ field by applying a dynamically thresholded image processing algorithm (Otsu, 1979). For each pixel and for a given time stamp, this method separates the surrounding pixels within a circular footprint of 5 km^2 into two classes, cell (foreground) and not-a-cell (background) and determines the dynamic threshold by minimizing intra-class intensity variance. More details of the cell identification algorithm can be found in Material S1. The diagrams in Figure S1.1 illustrate the operation of image thresholding, while Figure S1.2 demonstrates the operation of the cell identification algorithm. The resulting dynamic-thresholding has its advantages over using a fixed threshold value. Firstly, developing cells can be identified at lower reflectivity values. Additionally, individual

convective cells can be identified when embedded within a region of high reflectivity. Z_{DR} columns tend to be quite localized and are usually collocated within or near individual narrow updrafts that can develop before or during the occurrence of high radar reflectivity (Kennedy et al., 2001). It is therefore useful to study Z_{DR} columns within tracked cells using a dynamic threshold. Finally, the identified convective cells were tracked using an object-based algorithm developed by Stein et al. (2015). In brief, horizontal motion vectors are derived from previous images to displace the convective cells and cells inherit the identification number and properties of prior cells that have sufficient overlap. With the ability to track objects, we can consider the temporal evolution of Z_H and Z_{DR} within each tracked convective cell.

3.3 | Z_{DR} column detection algorithm

Since Z_{DR} columns are defined to intersect the freezing level, its height has to be found first before we identify such columns. The Met Office Unified Model (UM) has a global configuration that provides deterministic forecast covering a 6-day period. The model has a resolution of approximately 0.234×0.153 degrees of latitude and longitude respectively. Model runs occur every 12 h at 0 and 12UTC with forecast available every 3 h from T + 0 to 60 h. The temperature field is available every 12 h on standard pressure levels (i.e. 1000, 950, 925, 850, 700, 500, 400, 300, 250, 200, 150 and 100 hPa). The pressure level parameters used in this study are geopotential height and temperature at all standard pressure levels.

For each generated radar composite, the freezing level is determined by first finding the closest model run in time occurring before the valid time of the radar composite. The closest available time step within that model run is then selected for calculation of the freezing level. With the given geopotential heights and corresponding temperatures for the 12 standard pressure levels, geopotential heights are linearly interpolated to derive geopotential heights where air temperature is 0°C over the spatial domain of the radar composite. Mittermaier and Illingworth (2003) have confirmed that the UM predicts the wet-bulb zero within the specified 200 m error when compared with observations. While we speculate that the model will have improved since then, this error is smaller than the vertical resolution of the radar composite and thus suitable for this study.

With freezing heights calculated, we can now define the base of potential Z_{DR} columns within the 3D radar composite. The detection algorithm uses a primary Z_H threshold of 10 dBZ and primary Z_{DR} threshold of 1.0 dB to generate a 3D contiguous volume that extends at least 500 m above the freezing level to be considered a Z_{DR} column candidate. These primary thresholds are the same as those used in Plummer et al. (2018), whereas the study by Snyder et al. (2015) uses a $Z_{DR} \geq 1.0$ dB-only criterion with spatial filtering and despeckling to remove noisy signals such as ice along the edge of anvils. A candidate is then classified as a column if the maximum Z_H and maximum Z_{DR} within the volume exceed what we will refer to as secondary thresholds. These secondary thresholds of Z_H and Z_{DR} can be equal to or higher than the fixed primary thresholds to ensure well-defined column structures are identified, while eliminating noisier data. A visual comparison of Z_{DR} columns detected with or without the use of secondary thresholds can be found in Figure S2.1 of Material S2. An analysis on the choice of secondary thresholds will be explored in the following section.

3.4 | Example of Z_{DR} column detection

The 12 panels in Figure 4 show radar composite generated MAXDBZ plots covering a 30×40 km region in south-east England, indicated in Figure 4a. These plots show the case of a developing storm cell on 20 July 2021 and are overlaid with Z_{DR} column detection field shown as black pixels. In these detections, secondary thresholds of Z_H and Z_{DR} in the algorithm were set to 25 dBZ and 2.5 dB, respectively, as per the thresholds used in Plummer et al. (2018). The storm cell contained multiple Z_{DR} column detections starting from 1310Z and eventually grew into a storm containing MAXDBZ exceeding 50 dBZ at 1335Z. Flooding associated with the storm was recorded in mid-Kent and was reported by multiple news outlets (e.g. Mcconnell, 2021). The flash floods were also documented as a flooding event in the European Severe Weather Database (Dotzek et al., 2009).

Figure 5 visualises the Z_{DR} column detections within the blue rectangle domain at 1310Z with meridional and zonal cross sections. Figure 5a shows a vertical maximum plot of Z_H with accompanying cross sections. Figure 5b is the same plot but for Z_{DR}. These plots clearly show a contiguous volume of enhanced Z_{DR} exceeding 3.0 dB extending up to around 6 km in height, corresponding to 3 km above the environmental freezing level on that day. The identified feature is also associated with reflectivity values of 30 dBZ consistent with the automatically detected Z_{DR} columns in Figure 4.

4 | RESULTS

4.1 | Time series analysis

To test whether Z_{DR} columns are of use for early detection of severe weather, we first analyse the time series of

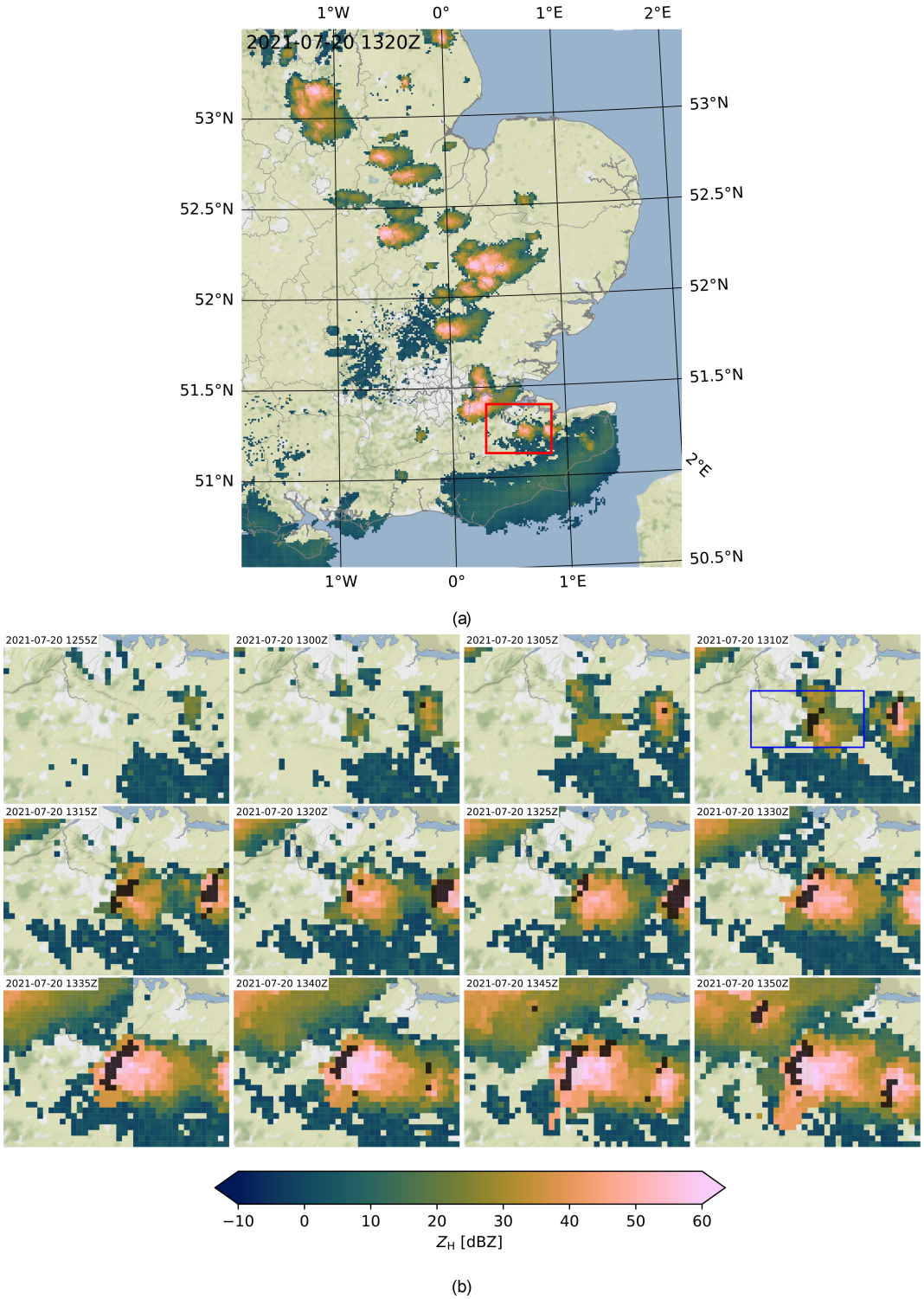

FIGURE 4 (a) An overview plot of MAXDBZ over eastern England on 20 July 2021 at 1320Z. The red rectangle demarcates a domain of interest with a convective storm development case. (b) A series of MAXDBZ showing convective storm development within the red rectangle domain for 20 July 2021 from 1255 to 1350Z. Panels in (b) are radar composites generated 5 min apart. Black pixels are detections of Z_{DR} columns. The blue rectangle in the 1310Z plot demarcates the region of the cross section of a convective cell in Figure 5. Map tiles by Stamen Design, under CC BY 4.0. Data by OpenStreetMap, under ODbL.

tracked cells for the time between Z_{DR} column detection and onset of severe weather as defined using MAXDBZ described in Section 2.1.

Figure 6 shows a composite time series analysis of accumulated MAXDBZ pixels and accumulated Z_{DR} column pixels within tracked storms. We accumulate the

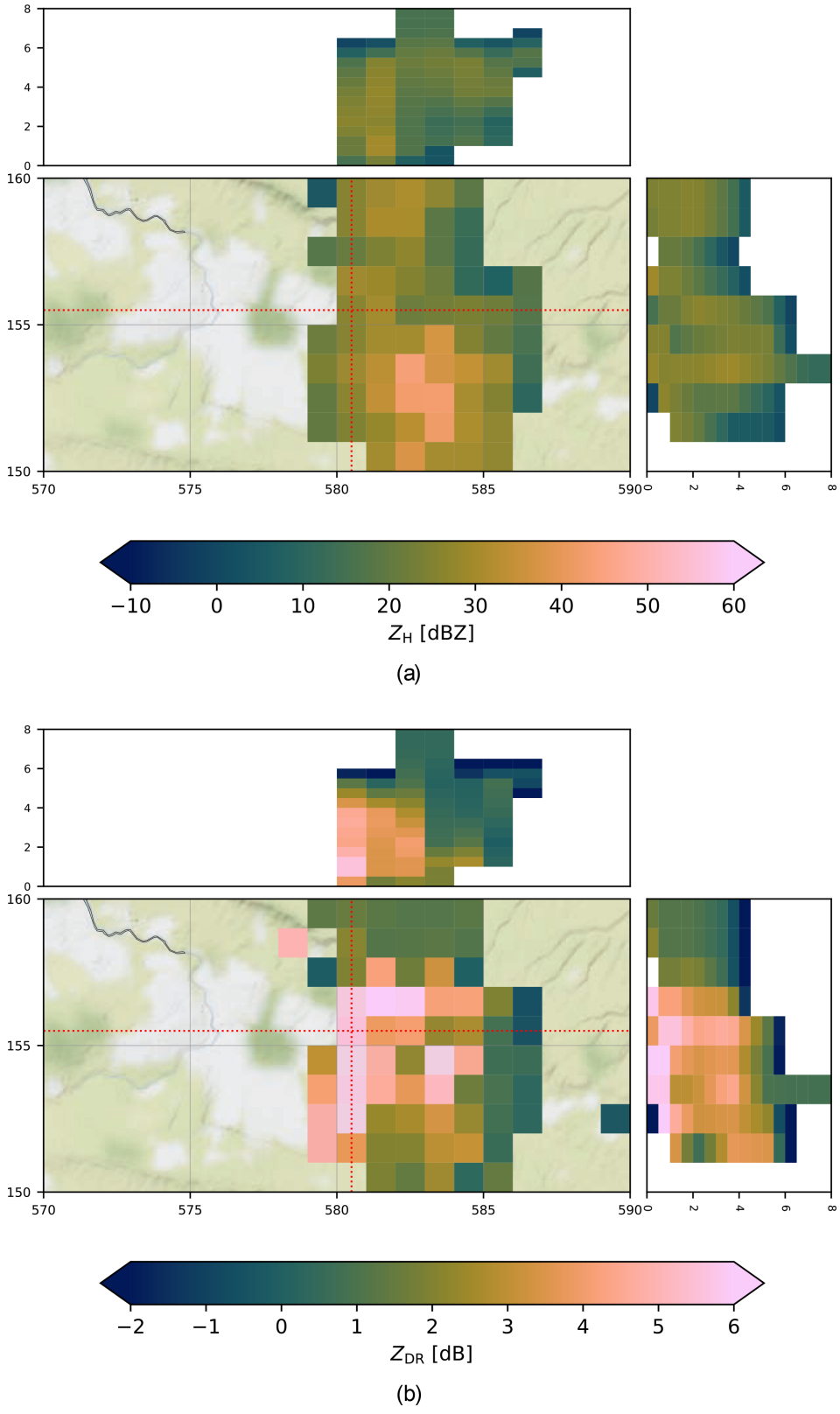

FIGURE 5 (a) A maximum Z_H plot with vertical cross sections on 20 July 2021 at 1310Z. Red dotted lines show the position of the vertical cross sections. Vertical cross section plots have 2 km tick labels in height. Spatial domain covered is the blue rectangle in Figure 4b, 1310Z panel. Enhanced Z_{DR} values exceeding 3.0 dB are present near the western flank of the cell suggesting the presence of a Z_{DR} column. (b) As in (a), but for Z_{DR}. The Z_{DR} column is accompanied by reflectivity values not exceeding 30 dBZ. Map tiles by Stamen Design, under CC BY 4.0. Data by OpenStreetMap, under ODbL.

number of Z_{DR} column pixels as well to test the importance of size and persistence of the Z_{DR} column for severe weather detection. Note that we only consider Z_{DR} column footprints, not the volume of 3D Z_{DR} observations. Only tracked storms that had both Z_{DR} column pixels and were eventually labelled as severe were included in this analysis; missed storms and false alarms will be considered in the next sub-section. Zero lead time is defined as the time when the definition of severe was met by the tracked cell. The choice of accumulated Z_{DR} pixels is in

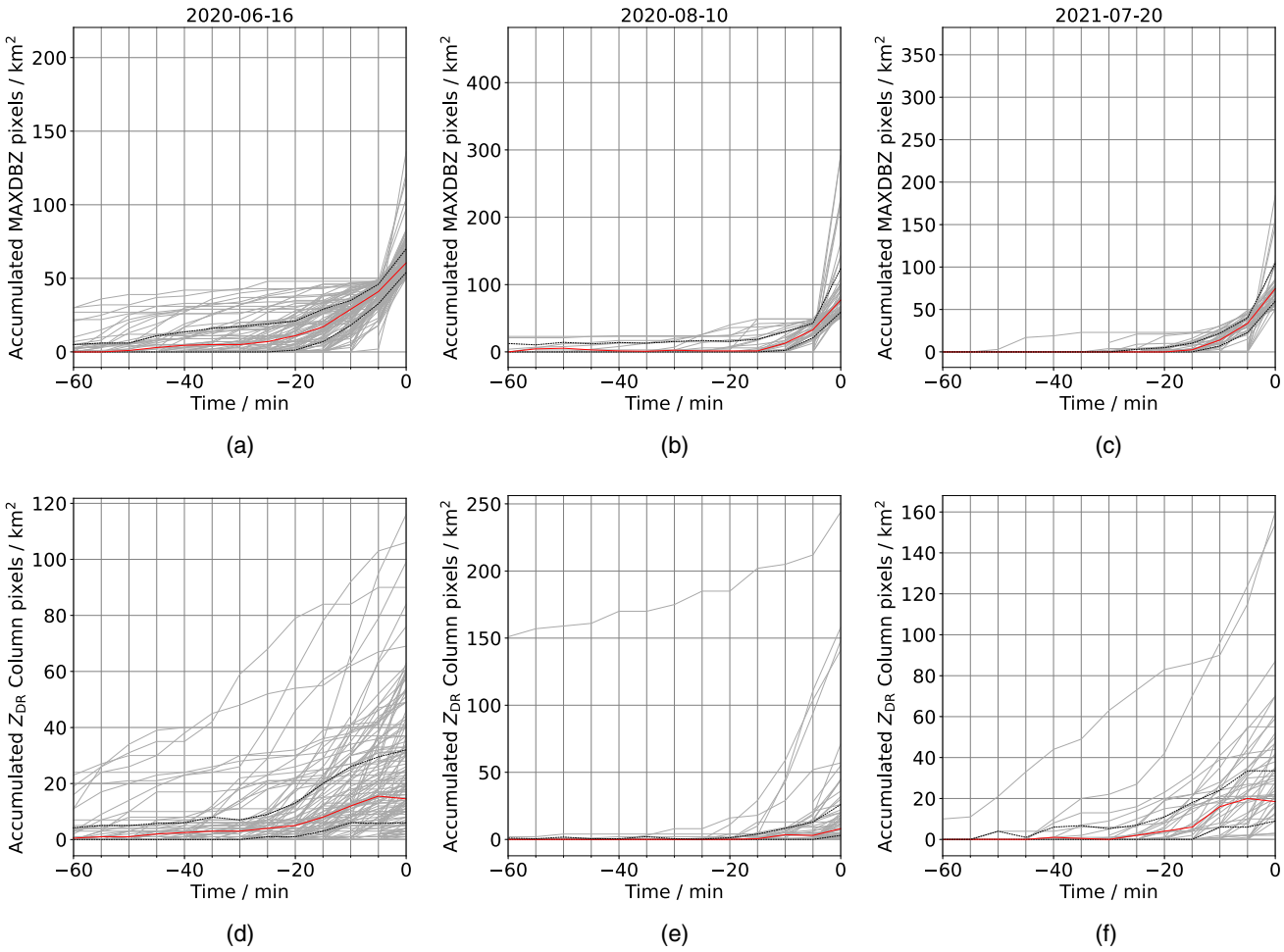

FIGURE 6 Grey lines showing time series of tracked storm properties in each case. Zero time is defined as the tracked storm meeting 50 accumulated pixels of MAXDBZ. In each sub-figure, upper panels (a–c) show MAXDBZ pixels within a tracked storm, whereas lower panels (d–f) show the accumulated number of detected Z_{DR} column pixels within each tracked storm. Red and black dotted lines show the median and quartiles of the time series, calculated from available data at each 5 min time step. First (a and d), second (b and e) and third (c and f) column of panels correspond to storms tracked on 16 June 2020, 10 August 2020 and 20 July 2021.

contrast to several past studies that have used column properties such as their heights, volume, area and maximum Z_{DR} value within the column. Past observational studies such as Kuster et al. (2020) have focused on measuring column properties by utilizing a bespoke rapid-scan strategy and is therefore not characteristic of what could be done operationally with the UK radars used in this study. Snyder et al. (2015) used operational data from the NEXRAD WSR radars that scan at higher elevation angles, enabling them to report the heights of Z_{DR} columns defined as the height of $Z_{DR} \geq 1.0$ dB at each pixel. In contrast, we are interested more in the persistence of Z_{DR} columns rather than their vertical extents. We are also limited by the compositing process, which may use information from radar ranges exceeding 100 km and hence larger beam sampling volume with uncertainty in the vertical on the order of 1 km. While on a "storm object" basis, Z_{DR} column information could be reasonable; its height is not reliable on a pixel-by-pixel basis. Stein et al. (2020) also found quite a large root-mean-square error in heights of reflectivity contours within the radar composite but with only a small bias. This further suggests the suitability of using aggregate information over instantaneous measurements. Past modelling studies (e.g. Kumjian et al., 2014) were able to measure column properties accurately at higher spatial resolutions. However, in this study, we are limited to a horizontal resolution of 1 km. Rather than studying the properties of each Z_{DR} column signature, the reasons provided justify using an accumulated metric to ensure robustness of a possible Z_{DR} column or multiple of them occurring within a tracked convective cell.

For the cases of 16 June 2020 (Figure 6a,d) and 20 July 2021 (Figure 6c,f), the median and upper quartiles show

a clear signal of 10–20 km^2 of Z_{DR} column pixel accumulation before time zero. Both cases see the steepest increases in Z_{DR} column pixel accumulation at approximately 10–20 min of lead time. For the case on 10 August 2020 (Figure 6b,e), the accumulation of Z_{DR} column pixels in the median time series at zero time is lower, at 8 km^2 compared with 14.5 and 18 km^2 for the other two cases, although the upper quartile time series is comparable across all three cases.

To consider the importance of size and duration of the Z_{DR} column, Figure 7 shows box plots of lead time, which is the duration between tracked storms meeting a certain threshold of accumulated Z_{DR} column pixels and meeting our radar-based definition of severe convection. Note that when we increase our threshold of accumulated Z_{DR} column pixels, we also reduce the sample going into these statistics, thus increasing the number of missed events. For all cases, lead time decreases with increasing Z_{DR} column number threshold. This is expected since tracked storms should accumulate an increasing number of detected Z_{DR} column pixels throughout their lifetimes, such that a larger accumulation of such pixels is likely to occur closer in time to the occurrence of high-reflectivity pixels. The spread of lead times also decreases when using a higher Z_{DR} column pixel threshold. Long lead times could also suggest the possibility for a long-lived storm that had Z_{DR} columns early in its lifetime but only later redeveloped into an intense storm that met our definition of severe convection. Thus, using a higher threshold of Z_{DR} column detection (e.g. 10 pixels) would suggest better robustness of Z_{DR} column detection, despite a shorter lead time. Z_{DR} columns are typically associated with vigorous updrafts that evolve into areas of high-reflectivity cores associated with greater concentrations of hail and large freezing raindrops. This conceptual model is supported by observations and modelling studies (e.g. Knight, 2006; Kumjian et al., 2014) that suggest Z_{DR} columns to precede the occurrence of high reflectivity up to 30 min in advance, although other studies such as Picca et al. (2010) may have found longer lead times of 40 min between Z_{DR} column detection and large hail diagnosis in some convective cells. It is worth noting, however, that our study covers a broader definition of severe convective weather not limited to hail.

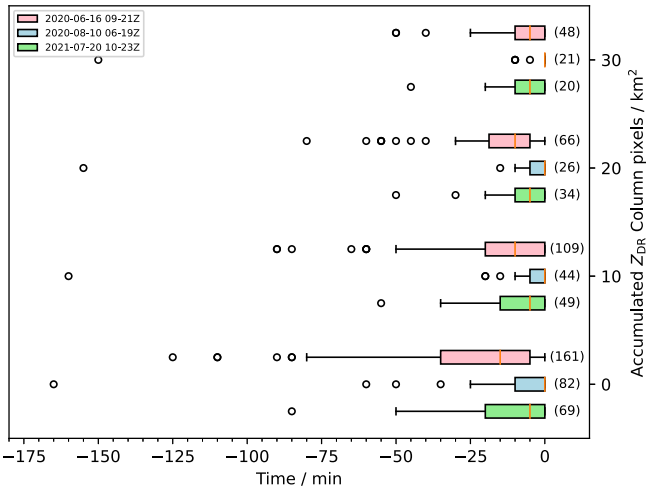

FIGURE 7 Box plots showing tracked storms that have met an accumulated Z_{DR} column pixel threshold and later lead to severe storm development. Lead time is the time between accumulated Z_{DR} column pixel threshold being met and the time when the tracked storm meets the severe requirement. Whiskers extend from the quartiles by 1.5 times the inter-quartile range. Tracked storms with longer lead times are marked as circles beyond the whiskers. Box plots are grouped according to accumulated Z_{DR} column pixel threshold and sub-divided by different cases. Red, blue and green shading correspond to storms tracked on 16 June 2020 from 09 to 21Z, 10 August 2020 from 06 to 19Z and 20 July 2021 from 10 to 23Z respectively. The number of elements for each box plot is shown in parentheses.

For the same accumulated Z_{DR} column pixel threshold, we also observe variations in lead time between the three cases considered. Considering a Z_{DR} column pixel threshold of 10, the upper quartile lead times are 20, 5 and 15 min for 16 June 2020, 10 August 2020 and 20 July 2021 cases, respectively. This shows differences in the time of Z_{DR} column appearance within storm evolution between case days with varying synoptic situation, complicating any algorithm design using Z_{DR} columns for nowcasting.

4.2 | Nowcasting verification

To investigate the skill of Z_{DR} column detection as a precursor of severe convection, non-precursor and non-severe events must also be considered. In addition to counting tracked storms with Z_{DR} column detection, a 2×2 contingency table is constructed to tally the number of tracked storms with Z_{DR} columns detected that did not later develop into a severe storm (false alarms), tracked storms without a Z_{DR} column precursor but later considered to be a severe cell (misses) and cells without a Z_{DR} column precursor and any remaining storms (correct negatives). From the number of hits (A), false alarms (B), misses (C) and correct negatives (D), verification metrics are calculated such as probability of detection (POD $= A/(A+C)$), false alarm ratio (FAR $= B/(A+B)$) and critical success index (CSI $= A/(A+B+C)$). CSI lacks any dependence on the number of correct negatives, which makes it suitable as a performance measure for rare events. As mentioned in Section 3.2, a cell is a contiguous area of MAXDBZ pixels above the variable

"Otsu" threshold or 20 dBZ, whichever is higher, and a severe event as having accumulated 50 pixels over 50 dBZ, as described in Section 2.1. To confirm that these severe convective events are rare, we find base rates of 0.9%, 0.4% and 1.6% meeting the severe definition out of all tracked storms for the 16 June 2020, 10 August 2020 and 20 July 2021 case days, respectively.

To inform future development of nowcasting algorithms using Z_{DR} columns, we are also interested in the sensitivity of the detection algorithm to the various thresholds introduced, particularly (a) the secondary Z_H threshold, (b) the secondary Z_{DR} threshold and (c) the Z_{DR} column accumulation threshold. All three of these thresholds will affect the contingency table, with higher thresholds moving hits to misses and false alarms to correct negatives. Informed by Section 4.1 and Figure 7, our severe weather precursor requires 10 accumulated Z_{DR} column pixels between 5 and 30 min prior to the definition of severe weather being met within a tracked convective cell. The choice of this 30-min threshold was informed by the box plot of precursor lead times in Figure 7 showing most storms having precursor lead times of <30 min. We note that this 30-min threshold considers lead times between 5 and 30 min, rather than storms meeting the severe definition beyond 30 min of having accumulated 10 Z_{DR} column pixels. Higher values of Z_H and Z_{DR} are considered more stringent secondary thresholds, since drops with even more oblateness are required in the storm for detection of a Z_{DR} column. This will lead to fewer storms labelled with precursors and more missed severe weather events, but also a decreased amount of false alarms.

Figure 8 shows the performance of the detection algorithm in nowcasting severe convective events by varying the secondary thresholds of Z_H and Z_{DR} for the cases of 16 June 2020, 10 August 2020 and 20 July 2021 respectively. For determining the significance of verification metrics presented, bootstrapping was carried out using secondary thresholds of 25dBZ and 2.5 dB for the detection of Z_{DR} columns. This gives an estimate of the uncertainties for the corresponding verification metric across secondary threshold space of Z_H and Z_{DR}. In all three cases, POD decreases with increasing secondary thresholds. Going from thresholds of $Z_{DR} \geq 1$ dB and $Z_H \geq 18$ dBZ to $Z_{DR} \geq 2$ dB and $Z_H \geq 30$ dBZ reduces POD from around 0.47 to 0.38 in the June case. Likewise, we see a reduction in POD from 0.19 to 0.10 in the August case. In contrast, the July case shows fairly constant POD values of around 0.40. However, the reduction in FAR is greatest in the August case, from 0.77 to 0.65, followed by the July case from 0.43 to 0.36, whereas these are fairly constant with values around 0.50 for the June case.

A common metric used to assess the ability to forecast rare severe weather events is the CSI, also known as threat score. For each studied case day, choosing secondary thresholds of $Z_{DR} = 1.4$ dB and $Z_H = 30$ dBZ would provide the highest CSI values, resulting in 0.28, 0.11 and 0.33. These values are lower than other nowcasting studies such as Seroka et al. (2012) that achieved CSI of up to 0.45 in cell-based verification when reflectivity was used to predict cloud-to-ground lightning.

We see differences in the distribution of CSI values across the secondary threshold space. The case of 10 June 2021 had the highest CSI around 1.0–1.6 dB of Z_{DR} and 10–26 dBZ of Z_H secondary thresholds. These values of Z_{DR} and Z_H are consistent with previous physical understanding that Z_{DR} columns consist of a low concentration of large drops present in growth stage of storms with updrafts later leading to severe convection.

The case of 10 August 2020 presents a different profile of maximum CSI extending to higher Z_H thresholds exceeding 30 dBZ although with a slightly narrower range of Z_{DR} thresholds between 1.0 and 1.4 dB. This is associated with the highest hit cases concentrated in the lower secondary Z_H Z_{DR} thresholds and significant decrease in false alarm cases as evidenced by the drop in FAR from 0.77 to 0.59 across tested Z_H thresholds. Similar to the June case, enhanced Z_{DR} thresholds are consistent with expected Z_{DR} column microphysics. The sensitivity of FAR across Z_H but less so in Z_{DR} suggests that the detection of Z_{DR} columns consisting of a higher concentration of raindrops resulted in a lower amount of tracked cells falsely predicted to meet the definition of severe convection.

The case of 20 July 2021 presents maximum CSI values that do not vary much over both Z_{DR} and Z_H. This is similar to the rather constant POD and FAR values over tested secondary thresholds. Similar to the August case, enhanced Z_{DR} thresholds are consistent with expected Z_{DR} column microphysics. However, the insensitivity of the POD metric to Z_H could suggest hail development in most tracked severe cells. The possible presence of hail within detected Z_{DR} columns in cells tracked on this day will be detailed later. In the August case, high CSIs were dominated by the hit cases mostly described by low thresholds and a marked decrease of false alarms with increasing Z_H. In this case, the number of hits (~30) and misses (~42) for Z_{DR} thresholds <2.0 dB were fairly constant. Despite there being a decrease in false alarms for increasing Z_H, there was no significant increase in CSI.

To explore the possibility of hail growth in Z_{DR} columns, we use a hail diagnostic based on the polarimetric algorithm of Aydin et al. (1986). The diagnostic H_{DR} is a function of Z_H and Z_{DR} (See equations 4 and 5 in Aydin et al. (1986) for more details). Any positive H_{DR} could

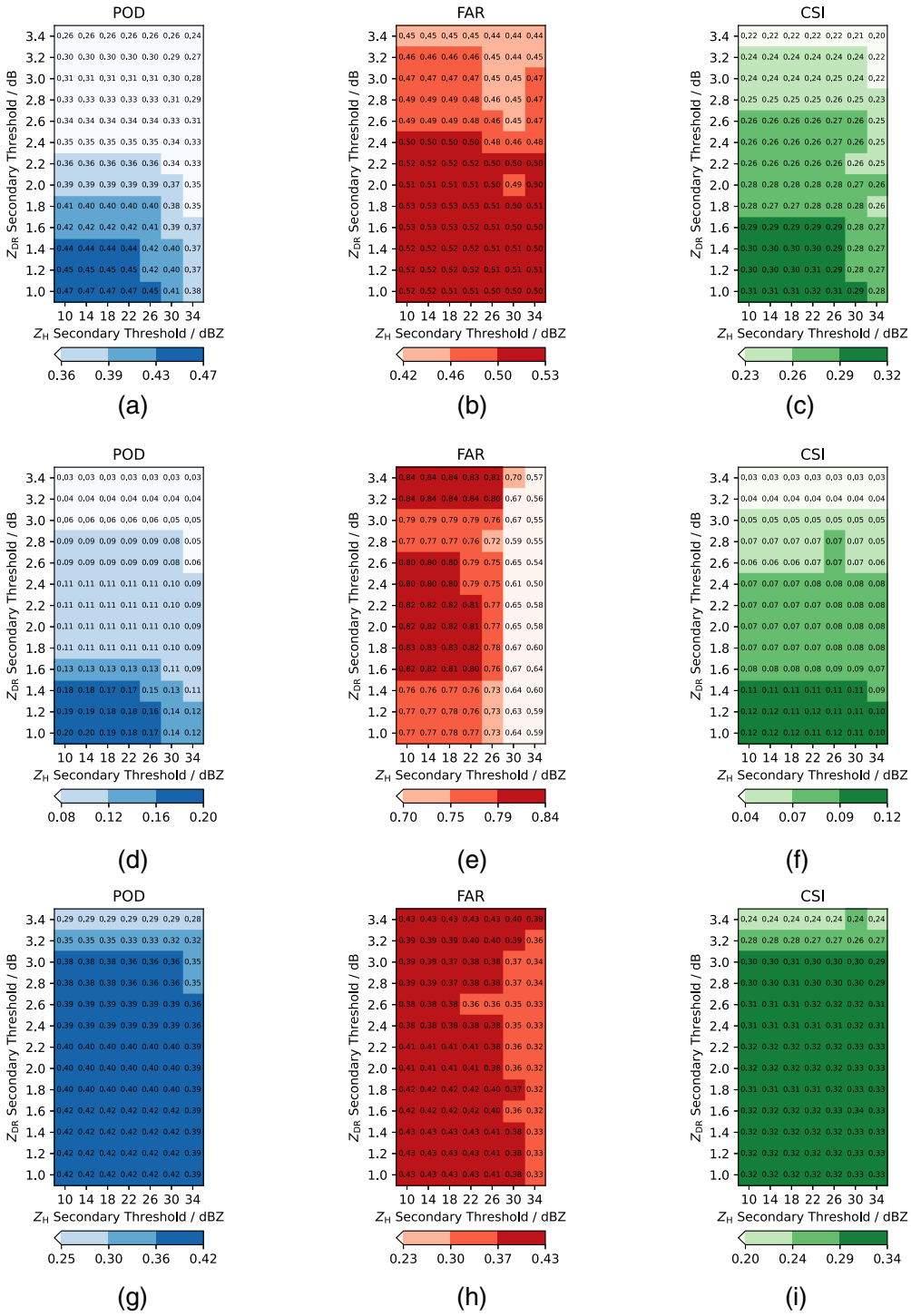

FIGURE 8 Verification metrics for verifying the effectiveness of Z_{DR} column appearance prior to severe convection for tracked storms on (a–c) 16 June 2020, (d–f) 10 August 2020 and (g–i) 20 July 2021 showing how probability of detection (POD), false alarm rate (FAR) and critical success index (CSI) varies over changing secondary reflectivity and differential reflectivity thresholds in Z_{DR} column detection algorithm. $N = 18{,}605$, 24,723 and 4476 convective cells were tracked for 16 June 2020, 10 August 2020 and 20 July 2021, respectively. From bootstrapping tracked storms at 25 dBZ of Z_H and 2.5 dB of Z_{DR}, each colour level represents one standard deviation of change in the verification metric.

signify the presence of hail, with larger values providing more certainty that the signal is not due to raindrops. Depue et al. (2007) found an H_{DR} threshold of 30 dB to be most reliable when tested against hail damage reports. We thus chose this threshold of $H_{DR} \geq 30$ dB to identify the potential presence of hail flagging columns in the radar

composite where the maximum H_{DR} reaches above this threshold. Figure 9b,d,f shows where hail was identified using this approach for 16 June 2020, 10 August 2020 and 20 July 2021 cases, respectively. A small frequency of hail was diagnosed for the June case with 9185 pixels of Z_{DR} columns and 196 pixels of hail. Hail was diagnosed in isolated regions in the August case with 11,104 pixels of Z_{DR} columns and 240 pixels of hail. Z_{DR} columns diagnosed in this case over the Celtic Sea and Ireland may not be reliable owing to coverage by only one or two radars. In the July case, hail diagnosis was more widespread with 3506 pixels of Z_{DR} columns and 1049 pixels of hail. In this final case, the hail diagnostics were collocated with many regions of Z_{DR} column detection.

Reviewing Figure 8 with the knowledge that the July case has hail present, we can consider how that could affect the CSI pattern. In particular, a storm with hail present is highly likely to be severe (50 accumulated MAXDBZ pixels above 50dBZ) and has a high Z_H. For the July case, we see that the whole range of tested Z_H thresholds lead to little changes in POD, FAR and CSI, especially for Z_{DR} secondary thresholds of less than 2.0 dB. Analysis of further cases will be necessary to disentangle the Z_{DR} column detection from hail contamination and explore the need for an algorithm that can warn of both heavy rainfall and hail. It is also possible that different environmental conditions may have led to air parcels containing different drop size distributions with

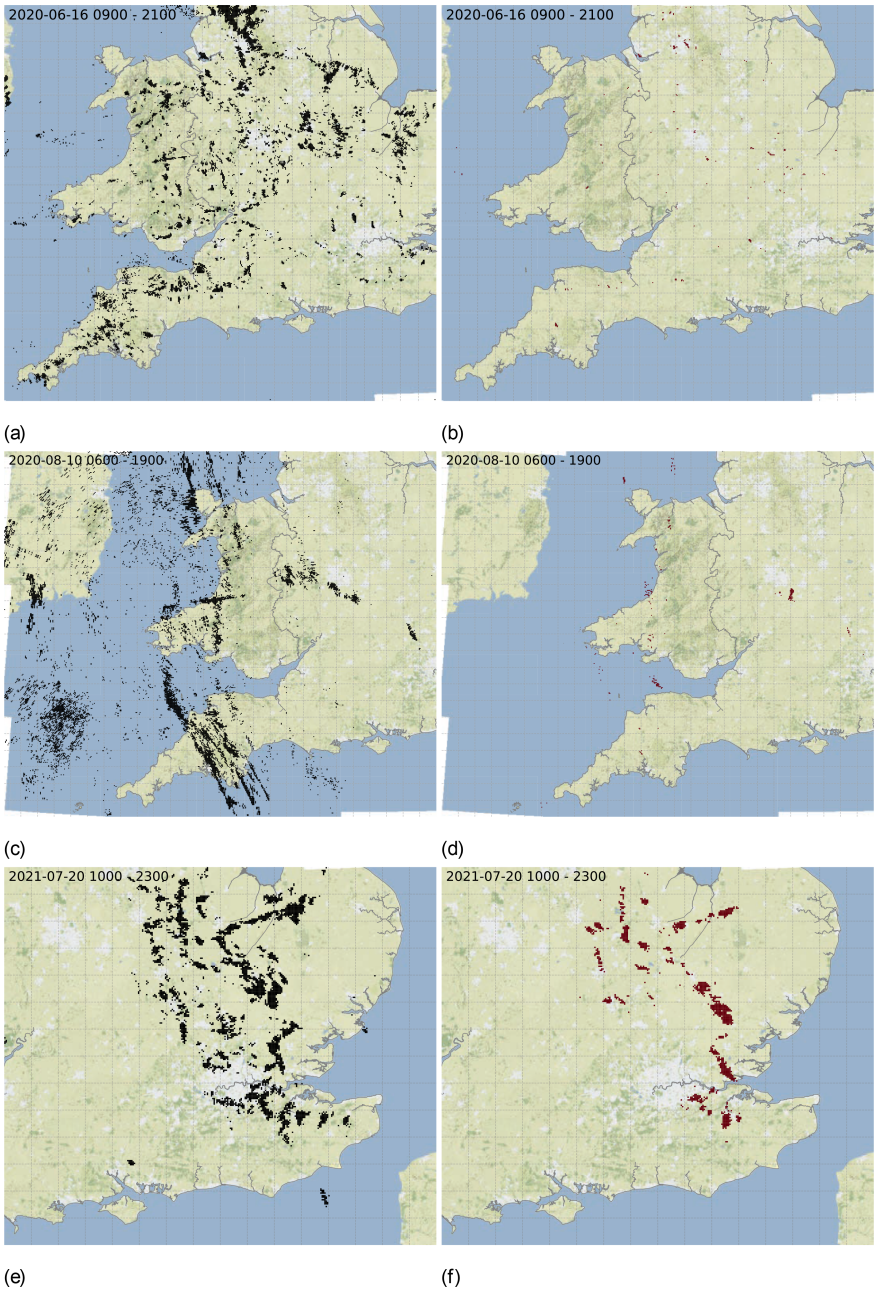

FIGURE 9 The left panels show accumulated detections of Z_{DR} columns using secondary thresholds of 2.5 dB and 25 dBZ Z_{DR} and Z_H, respectively, over the case days of (a) 16 June 2020, (c) 10 August 2020 and (e) 20 July 2021. The right three panels (b), (d) and (f) are accumulations of the hail diagnostic from Aydin et al. (1986) applied to the same three cases respectively. Brown areas indicate hail signals exceeding a vertical maximum of H_{DR} equal or exceeding 30 dB. Map tiles by Stamen Design, under CC BY 4.0. Data by OpenStreetMap, under ODbL.

higher concentrations of smaller drops resulting in enhanced Z_H.

5 | DISCUSSION AND CONCLUSIONS

A three-dimensional radar composite comprising data from polarimetric C-band radars was used for identifying Z_{DR} columns over the United Kingdom. The identification algorithm was tested for its ability in nowcasting severe convection, which was for this UK study defined as accumulating 50 km^2 pixels with MAXDBZ >50 dBZ over the lifetime of the cell.

Using image thresholding and object tracking techniques, storm timelines were derived. A lead-time analysis on these timelines found up to 20 min of lead time between an increase in the number of detected Z_{DR} column pixels and the tracked cell meeting the criterion for severe convection. However, it is worth noting the variability in lead time depending on the considered case and the accumulated Z_{DR} pixels used as a criterion for diagnosis of severe convection. Although we do not consider column height in this article, our findings on lead time are comparable with storm cases in Kuster et al. (2020), where they found Z_{DR} column heights increasing 11 min prior to an increase in reflectivity within the cell, and in one case, Z_{DR} column development occurred 16 min prior to a hail report. Despite having different definitions of labelling storms as "severe" across studies due to differing storm morphologies and the occurrence of severe weather in different geographical regions, it is nevertheless promising to see how Z_{DR} columns act as precursors for severe convection.

Results from this study suggest that enhanced Z_{DR} values above 1.0 dB are suitable for Z_{DR} column detection within storms that lead to severe convection in the United Kingdom. Although this is similar to the implementation in Snyder et al. (2015), we also implemented an additional primary threshold of $Z_H \geq 10$ dBZ to exclude noisy data and ice in stratiform cloud that could be mistaken for a Z_{DR} column. The need for secondary thresholds, as justified in Plummer et al. (2018), ensures the identification of subjectively well-defined column structures.

The use of verification metrics, such as CSI, in exploring secondary threshold space highlighted appropriate Z_{DR} and Z_H values for each case day. We were able to attribute the best algorithm performance for a wider spread of Z_H secondary thresholds to hail presence within detected Z_{DR} columns. In contrast to Plummer et al. (2018) who used secondary thresholds of 2.5 dB and 25 dBZ Z_{DR} and Z_H thresholds respectively for detecting Z_{DR} columns, our results suggest that preferred Z_{DR} secondary threshold be lower at 1.4 dB and a similar Z_H secondary threshold at 30 dBZ. We note, however, that the set of secondary thresholds that offer the best algorithm performance varies amongst cases.

Our study highlights several issues with using Z_{DR} columns to nowcast severe convection. Our POD ~0.40 could be comparable with other studies, but similarly high FARs could consequently lead to lower CSIs. Potentially, additional criteria on the Z_{DR} column height could reduce the FAR and these are in line with the physical interpretation of Z_{DR} columns. However, for the UK composite, heights above 3 km are generally observed by low-elevation scans at ranges >100 km. At such ranges, the beam widths are >1 km leading to uncertainty in estimating Z_{DR} column height. A comparison of Z_{DR} columns in the composite against a research grade radar such as CAMRa might help (e.g. Stein et al., 2020), but the rarity of these events makes this a challenging task. Scan strategies involving higher elevations would also provide better coverage at higher altitudes. This would permit a more reliable measurement of Z_{DR} column heights, which could potentially be exploited as an additional identification criterion. Considering that data latency of producing a radar composite output is of similar magnitude to the median lead times of Z_{DR} column accumulation, we also acknowledge there to be some practical applicability of Z_{DR} columns as a precursor in the Met Office's operational setting at least based on the three cases presented here.

The question of whether a consistent set of thresholds can be found and whether Z_{DR} columns are more prominent at a similar range of lead times before the onset of severe weather in certain synoptic conditions could be of interest in future studies. The availability of the polarimetric data for the United Kingdom to capture more case days of interest will allow future work to build on existing synoptic regime analysis (e.g. Wilkinson & Neal, 2021) and Z_{DR} column prevalence within convective storms.

AUTHOR CONTRIBUTIONS

Chun Hay Brian Lo: Conceptualization (equal); formal analysis (lead); funding acquisition (lead); investigation (lead); methodology (equal); project administration (equal); software (lead); visualization (lead); writing – original draft (lead); writing – review and editing (equal). **Thorwald H. M. Stein:** Conceptualization (equal); methodology (equal); project administration (equal); resources (equal); supervision (lead); writing – original draft (supporting); writing – review and editing (equal). **Robert W. Scovell:** Conceptualization (equal); methodology (equal); resources (equal); supervision (supporting);

writing – original draft (supporting); writing – review and editing (supporting). **Chris D. Westbrook:** Conceptualization (equal); methodology (equal); project administration (supporting); supervision (supporting); writing – original draft (supporting); writing – review and editing (supporting). **Timothy Darlington:** Resources (equal); supervision (supporting); writing – original draft (equal); writing – review and editing (equal). **Humphrey W. Lean:** Resources (equal); supervision (supporting); writing – original draft (supporting); writing – review and editing (supporting).

ACKNOWLEDGEMENTS

The authors of this manuscript would like to thank Matthew Lehnert for providing his knowledge on severe weather analysis from the perspective of a Met Office operational forecaster.

FUNDING INFORMATION

Chun Hay Brian Lo was supported by a scholarship from the Department of Meteorology at the University of Reading and a UK Met Office CASE Studentship.

CONFLICT OF INTEREST STATEMENT

All authors declare that they have no conflicts of interest.

DATA AVAILABILITY STATEMENT

Radar and Met Office global model data are available through the CEDA Archive. Further information about the data and conditions for access are available at: https://www.ceda.ac.uk/services/ceda-archive/.

PERMISSION TO REPRODUCE MATERIAL FROM OTHER SOURCES

The authors declare that they have permission to reproduce any previously published material.

ORCID

Chun Hay Brian Lo https://orcid.org/0000-0001-7661-7080
Thorwald H. M. Stein https://orcid.org/0000-0002-9215-5397

REFERENCES

Aydin, K., Seliga, T.A. & Balaji, V. (1986) Remote sensing of hail with a dual linear polarization radar. *Journal of Climate and Applied Meteorology*, 25, 1475–1484.

Brandes, E.A., Vivekanandan, J., Tuttle, J.D. & Kessinger, C.J. (1995) A study of thunderstorm microphysics with multiparameter radar and aircraft observations. *Monthly Weather Review*, 123, 3129–3143.

Depue, T.K., Kennedy, P.C. & Rutledge, S.A. (2007) Performance of the hail differential reflectivity (HDR) polarimetric radar hail indicator. *Journal of Applied Meteorology and Climatology*, 46, 1290–1301.

Dotzek, N., Groenemeijer, P., Feuerstein, B. & Holzer, A.M. (2009) Overview of ESSL's severe convective storms research using the European severe weather database ESWD. *Atmospheric Research*, 93, 575–586.

Harrison, D.L., Scovell, R.W. & Kitchen, M. (2009) High-resolution precipitation estimates for hydrological uses. *Proceedings of the Institution of Civil Engineers – Water Management*, 162, 125–135.

Herzegh, P.H. & Jameson, A.R. (1992) Observing precipitation through dual-polarization radar measurements. *Bulletin – American Meteorological Society*, 73, 1365–1374.

Hogan, R.J., Field, P.R., Illingworth, A.J., Cotton, R.J. & Choularton, T.W. (2002) Properties of embedded convection in warm-frontal mixed-phase cloud from aircraft and polarimetric radar. *Quarterly Journal of the Royal Meteorological Society*, 128, 451–476.

Hogan, R.J., Francis, P.N., Flentje, H., Illingworth, A.J., Quante, M. & Pelon, J. (2003) Characteristics of mixed-phase clouds. I: lidar, radar and aircraft observations from CLARE'98. *Quarterly Journal of the Royal Meteorological Society*, 129, 2089–2116.

Illingworth, A.J., Goddard, J.W. & Cherry, S.M. (1987) Polarization radar studies of precipitation development in convective storms. *Quarterly Journal of the Royal Meteorological Society*, 113, 469–489.

Kennedy, P.C., Rutledge, S.A., Petersen, W.A. & Bringi, V.N. (2001) Polarimetric radar observations of hail formation. *Journal of Applied Meteorology*, 40, 1347–1366.

Knight, C.A. (2006) Very early formation of big, liquid drops revealed by ZDR in continental cumulus. *Journal of the Atmospheric Sciences*, 63, 1939–1953.

Kumjian, M.R. (2013) Principles and applications of dual-polarization weather radar. Part II: warm- and cold-season applications. *Journal of Operational Meteorology*, 1, 243–264.

Kumjian, M.R., Khain, A.P., Benmoshe, N., Ilotoviz, E., Ryzhkov, A.V. & Phillips, V.T. (2014) The anatomy and physics of ZDR columns: investigating a polarimetric radar signature with a spectral bin microphysical model. *Journal of Applied Meteorology and Climatology*, 53, 1820–1843.

Kumjian, M.R. & Ryzhkov, A.V. (2008) Polarimetric signatures in supercell thunderstorms. *Journal of Applied Meteorology and Climatology*, 47, 1940–1961.

Kuster, C.M., Schuur, T.J., Lindley, T.T. & Snyder, J.C. (2020) Using ZDR columns in forecaster conceptual models and warning decision making. *Weather and Forecasting*, 35, 1–43.

Kuster, C.M., Snyder, J.C., Schuur, T.J., Lindley, T.T., Heinselman, P.L., Furtado, J.C. et al. (2019) Rapid-update radar observations of ZDR column depth and its use in the warning decision process. *Weather and Forecasting*, 34, 1173–1188.

Marshall, J.S., Langille, R.C. & Palmer, W.M.K. (1947) Measurement of rainfall by radar. *Journal of Meteorology*, 4, 186–192.

McConnell, E. (2021) Kent weather: thunderstorms and flooding hit parts of county. https://www.kentonline.co.uk/kent/news/thunderstorms-to-rock-parts-of-kent-250957/

Mittermaier, M.P. & Illingworth, A.J. (2003) Comparison of model-derived and radar-observed freezing-level heights: implications for vertical reflectivity profile-correction schemes. *Quarterly Journal of the Royal Meteorological Society*, 129, 83–95.

National Weather Service. (2017) Severe thunderstorms definitions. https://www.weather.gov/bgm/severedefinitions

Otsu, N. (1979) A threshold selection method from gray-level histograms. *IEEE Transactions on Systems, Man, and Cybernetics*, 9, 62–66.

Picca, J., Kumjian, M.R. & Ryzhkov, A.V. (2010) ZDR columns As a predictive tool for hail growth. In: *25th conference on severe local storms*. Denver, Colorado: American Meteorological Society, p. 11.3.

Plummer, D.M., French, J.R., Leon, D.C., Blyth, A.M., Lasher-Trapp, S., Bennett, L.J. et al. (2018) Radar-derived structural and precipitation characteristics of ZDR columns within warm-season convection over the United Kingdom. *Journal of Applied Meteorology and Climatology*, 57, 2485–2505.

Scovell, R.W. & Al-Sakka, H. (2016) A point cloud method for retrieval of high-resolution 3D gridded reflectivity from weather radar networks for air traffic management. *Journal of Atmospheric and Oceanic Technology*, 33, 461–479.

Seroka, G.N., Orville, R.E. & Schumacher, C. (2012) Radar nowcasting of total lightning over the Kennedy space center. *Weather and Forecasting*, 27, 189–204.

Snyder, J.C., Bluestein, H.B., Dawson, D.T. & Jung, Y. (2017) Simulations of polarimetric, X-band radar signatures in supercells. Part II: ZDR columns and rings and KDP columns. *Journal of Applied Meteorology and Climatology*, 56, 2001–2026.

Snyder, J.C., Ryzhkov, A.V., Kumjian, M.R., Khain, A.P. & Picca, J. (2015) A ZDR column detection algorithm to examine convective storm updrafts. *Weather and Forecasting*, 30, 1819–1844.

Stein, T.H., Scovell, R.W., Hanley, K.E., Lean, H.W. & Marsden, N.H. (2020) The potential use of operational radar network data to evaluate the representation of convective storms in NWP models. *Quarterly Journal of the Royal Meteorological Society*, 146, 2315–2331.

Stein, T.H.M., Hogan, R.J., Clark, P.A., Halliwell, C.E., Hanley, K.E., Lean, H.W. et al. (2015) The DYMECS project: a statistical approach for the evaluation of convective storms in high-resolution NWP models. *Bulletin of the American Meteorological Society*, 96, 939–951.

Weisman, M.L. & Klemp, J.B. (1982) The dependence of numerically simulated convective storms on vertical wind shear and buoyancy. *Monthly Weather Review*, 110, 504–520.

Westbrook, C.D., Illingworth, A.J., O'Connor, E.J. & Hogan, R.J. (2010) Doppler lidar measurements of oriented planar ice crystals falling from supercooled and glaciated layer clouds. *Quarterly Journal of the Royal Meteorological Society*, 136, 260–276.

Wilkinson, J.M. & Neal, R. (2021) Exploring relationships between weather patterns and observed lightning activity for Britain and Ireland. *Quarterly Journal of the Royal Meteorological Society*, 147, 2772–2795.

Zhang, J., Howard, K. & Gourley, J.J. (2005) Constructing three-dimensional multiple-radar reflectivity mosaics: examples of convective storms and stratiform rain echoes. *Journal of Atmospheric and Oceanic Technology*, 22, 30–42.

SUPPORTING INFORMATION

Additional supporting information can be found online in the Supporting Information section at the end of this article.

How to cite this article: Lo, C. H. B., Stein, T. H. M., Scovell, R. W., Westbrook, C. D., Darlington, T., & Lean, H. W. (2024). Use of Z_{DR} columns for early detection of severe convection within the operational radar network of the United Kingdom. *Meteorological Applications*, *31*(1), e2159. https://doi.org/10.1002/met.2159